



# Functional redundancy in *Candida auris* cell surface adhesins crucial for cell-cell interaction and aggregation

Received: 11 March 2024

Accepted: 14 October 2024

Published online: 25 October 2024

Tristan W. Wang <sup>1</sup>, Dimitrios Sofras <sup>2</sup>, Daniel Montelongo-Jauregui <sup>1</sup>, Telmo O. Paiva <sup>3</sup>, Hans Carolus <sup>2</sup>, Yves F. Dufrêne <sup>3</sup>, Areej A. Alfaifi <sup>1,7</sup>, Carrie McCracken <sup>4</sup>, Vincent M. Bruno <sup>5</sup>, Patrick Van Dijck <sup>2,6</sup> & Mary Ann Jabra-Rizk <sup>1,5</sup>

Check for updates

*Candida auris* is an emerging nosocomial fungal pathogen associated with life-threatening invasive disease due to its persistent colonization, high level of transmissibility and multi-drug resistance. Aggregative and non-aggregative growth phenotypes for *C. auris* strains with different biofilm forming abilities, drug susceptibilities and virulence characteristics have been described. Using comprehensive transcriptional analysis we identified key cell surface adhesins that were highly upregulated in the aggregative phenotype during in vitro and in vivo grown biofilms using a mouse model of catheter infection. Phenotypic and functional evaluations of generated null mutants demonstrated crucial roles for the adhesins Als4112 and Scf1 in mediating cell-cell adherence, coaggregation and biofilm formation. While individual mutants were largely non-aggregative, in combination cells were able to co-adhere and aggregate, as directly demonstrated by measuring cell adhesion forces using single-cell atomic force spectroscopy. This co-adherence indicates their role as complementary adhesins, which despite their limited similarity, may function redundantly to promote cell-cell interaction and biofilm formation. Functional diversity of cell wall proteins may be a form of regulation that provides the aggregative phenotype of *C. auris* with flexibility and rapid adaptation to the environment, potentially impacting persistence and virulence.

The newly emerged nosocomial pathogen *Candida auris* is associated with outbreaks of life-threatening invasive disease worldwide<sup>1–4</sup>. *Candida auris* exhibits several concerning features including persistent colonization of skin and nosocomial surfaces, high transmissibility and unprecedented level of multidrug resistance<sup>5–11</sup>. In fact, *C.*

*auris* is now the first fungal pathogen categorized as an urgent threat by the Center for Disease Control (CDC), making it mandatory to report isolation of *C. auris* in the United States<sup>10,12</sup>. Significantly, the World Health Organization ranks *C. auris* as a critical priority pathogen, highlighting its importance to public health<sup>13</sup>. While

<sup>1</sup>Department of Oncology and Diagnostic Sciences, School of Dentistry, University of Maryland, Baltimore, MD, USA. <sup>2</sup>Laboratory of Molecular Cell Biology, Department of Biology, KU Leuven, Leuven, Belgium. <sup>3</sup>Louvain Institute of Biomolecular Science and Technology, UCLouvain, Croix du Sud, 4-5, L7.07.07, Louvain-la-Neuve, Belgium. <sup>4</sup>Institute for Genome Sciences, University of Maryland School of Medicine, Baltimore, MD, USA. <sup>5</sup>Department of Microbiology and Immunology, School of Medicine University of Maryland, Baltimore, MD, USA. <sup>6</sup>KU Leuven One-Health Institute, KU Leuven, Leuven, Belgium. <sup>7</sup>Present address: Department of Restorative and Prosthetic Dental Sciences, College of Dentistry King Saud bin Abdulaziz University for Health Sciences, Riyadh, Saudi Arabia. e-mail: [Patrick.vandijck@kuleuven.be](mailto:Patrick.vandijck@kuleuven.be); [mrizk@umaryland.edu](mailto:mrizk@umaryland.edu)

virulence factors associated with *C. auris* infections are not fully understood, the fungus shares key characteristics common to *Candida* species, including thermotolerance and biofilm formation, although some characteristics are strain-dependent<sup>10,14–16</sup>. Biofilm formation contributes to antifungal tolerance among *Candida* species as a result of drug sequestration, and in *C. auris*, biofilm formation was shown to protect *C. auris* from triazoles, polyenes, and echinocandins<sup>17–19</sup>. One unique growth feature reported in some clinical isolates is cell aggregation, which in vitro was associated with differences in drug susceptibility and transcriptional changes induced by exposure to antifungals<sup>20</sup>. Aggregative isolates were also shown to have a higher capacity for biofilm formation than non-aggregative isolates<sup>16,18,20–22</sup>.

Fungal cell wall adhesins are crucial for adherence to surfaces and biofilm formation and have been recognized as major virulence factors in *Candida* species<sup>23</sup>. Adhesins also play a fundamental role in interactions of fungal cells with each other enabling switching from a unicellular lifestyle to a multicellular one<sup>18</sup>. In *Candida* species, most notably, cell adhesion involves a family of cell surface Als (agglutinin-like sequence) proteins with amyloid-like clusters that activate cell-cell adhesion under mechanical stress<sup>24,25</sup>. Identified polymorphisms enriched in weakly aggregating strains of *C. auris* were found to be associated with loss of cell surface proteins; furthermore, amplification of the subtelomeric adhesin gene *ALS4* was associated with enhanced adherence and biofilm formation<sup>26,27</sup>. In addition, cell aggregation was shown to increase at higher growth temperatures, suggesting that aggregation is a complex phenomenon that may be linked to the ability to form extracellular matrix and cell surface amyloids<sup>26,28</sup>.

In this study, we aimed to identify unique transcriptional signatures associated with the aggregative phenotype during biofilm growth. As the in vivo and in vitro situations may have different functional requirements, comparative RNA-sequencing analysis was performed on *C. auris* strains grown in vitro and in vivo using our mouse model of catheter infection. Analysis of differentially regulated genes identified key cell wall adhesin genes to be significantly upregulated in the aggregative strain, and functional analysis of generated null mutants identified an adhesin important for biofilm formation in vivo. As complementary roles for diverse adhesins have been reported in *C. albicans*<sup>29</sup>, we aimed to explore adhesin functional redundancy and binding complementation in *C. auris*, which was demonstrated by measuring cell-cell adhesive forces using single-cell atomic force spectroscopy. Functional diversity of cell wall proteins may be a form of regulation providing the *C. auris* aggregative phenotype with flexibility and rapid adaptation to the environment. Therefore, dissecting this aggregative phenotype is crucial for understanding the biology, evolution and pathogenesis of *C. auris*.

## Results

### Transcriptional analysis identifies key cell wall adhesins to be significantly upregulated in an aggregating *C. auris* strain under both in vitro and in vivo growth conditions

To understand the molecular mechanisms behind the differences observed in the biofilm-forming ability of the two *C. auris* phenotypes, comprehensive RNA-sequencing analysis was performed on cells from in vitro-grown biofilms. A total of 76 genes were identified to be differentially expressed ( $LFC \geq |1|$ ,  $FDR < 0.01$ ) between the aggregative AR0382 (B1109) and nonaggregative AR0387 (B8441) strains (Fig. 1A); 47 of the genes were more highly expressed in AR0382, whereas 29 genes were more highly expressed in AR0387 (Supplementary Data 1). Transcriptional analysis of in vivo grown biofilms recovered from catheters implanted in mice identified 259 genes that were differentially expressed ( $LFC \geq |1|$ ,  $FDR < 0.01$ ) between AR0382 and AR0387 (Fig. 1B); 206 of the genes were more highly expressed in strain

AR0382 whereas 53 genes were more highly expressed in AR0387 (Supplementary Data 2). In total, 23 genes were commonly more highly expressed in AR0382 in vitro and in vivo (Fig. 1C) (Supplementary Data 3); among those genes, 5 encode putative adhesins, including B9J08\_001458 and B9J08\_004112, which have since been annotated as *SCF1* and *ALS4112*, respectively in the *Candida* Genome Database. In addition, identified were several homologs of *C. albicans* genes with known roles in adhesion, including B9J08\_004109 (*IFF4109*) and B9J08\_004100 and B9J08\_004451, belonging to the *IFF/HYR1* family of adhesins (Fig. 1A, B). Interestingly, gene B9J08\_002136, an ortholog of the *C. albicans* transcription factor *WOR2* and key regulator of white-to-opaque switching<sup>30</sup>, was significantly under-expressed in strain AR0382 under both growth conditions (Fig. 1A, B). In this study, we focused on the two adhesins *Scf1* and *Als4112*.

### The *C. auris* *Scf1* adhesin contains a Flo11 protein domain and a serine-threonine-rich region similar to the *C. albicans* *Rbt1* adhesin

We initially identified gene B9J08\_001458 as an ortholog of the *C. albicans* *RBT1* gene in agreement with a previous report<sup>31</sup>; however, this gene has since been renamed *SCF1*<sup>28</sup>. In exploring the similarity between the *C. auris* *Scf1* and the *C. albicans* *Rbt1* adhesin, comparative analysis of protein domain organization was performed. This revealed a comparable structure for *C. auris* *Scf1* to that of the *C. albicans* *Rbt1* and the *S. cerevisiae* *Flo11* adhesins; specifically, a *Flo11* domain and a serine-threonine-rich region recognized by *Als4112*, were present in all three proteins (Fig. 2).

### Mutant strain *Δscf1* but not *Δals4112* is compromised in in vitro biofilm formation compared to the wild-type strain

Quantitative evaluation of biofilms based on metabolic activity demonstrated that the *Δscf1* mutant formed significantly reduced biofilm compared to the wild-type strain. In contrast, the *Δals4112* biofilm was comparable to that of the wild-type (Fig. 3A). The non-aggregative AR0387 wild-type strain was severely deficient in biofilm formation compared to AR0382, and deletion of either of the genes in AR0387 had no additional effect on adhesion and biofilm formation (Fig. S1A). Biofilms formed by the complemented strains of mutants of both genes (*Δscf1 + SCF1* and *Δals4112 + ALS4112*) were comparable to that of the wild-type strain (Fig. S2A).

### Both mutant strains *Δscf1* and *Δals4112* are significantly deficient in aggregation

Following the vortexing of cell suspensions, the AR0382 wild-type strain formed large aggregates rapidly settling into sediment (Fig. 3B, C). In contrast, mutants lacking the *Scf1* or *Als4112* adhesins formed no or minimally visible aggregates and cells remained mostly suspended (Fig. 3B, C). Comparative measurement of sedimentation rates of aggregates based on drop in absorbance readings over time demonstrated that unlike with the *Δscf1* and *Δals4112* mutants, the drop in absorbance for the wild-type strain was dramatic (Fig. 3D). No aggregation was seen with cells of the AR0387 wild-type strain (Fig. S1B, C). The complemented strains of mutants of both genes (*Δscf1 + SCF1* and *Δals4112 + ALS4112*) formed aggregates comparable to those formed by the wild-type strain (Fig. S2B).

### *Scf1* and *Als4112* adhesins have complementary and redundant roles in cell-cell adherence and aggregation

In order to explore whether the two highly expressed adhesins in the aggregative strain have complementary roles, the two mutant strains were mixed and cell-cell adherence and coaggregation were monitored visually and quantitatively. Where individually both mutants failed to aggregate, in combination, cells co-adhered strongly, forming aggregates comparable to those formed by the wild-type strain (Fig. 3B–D).

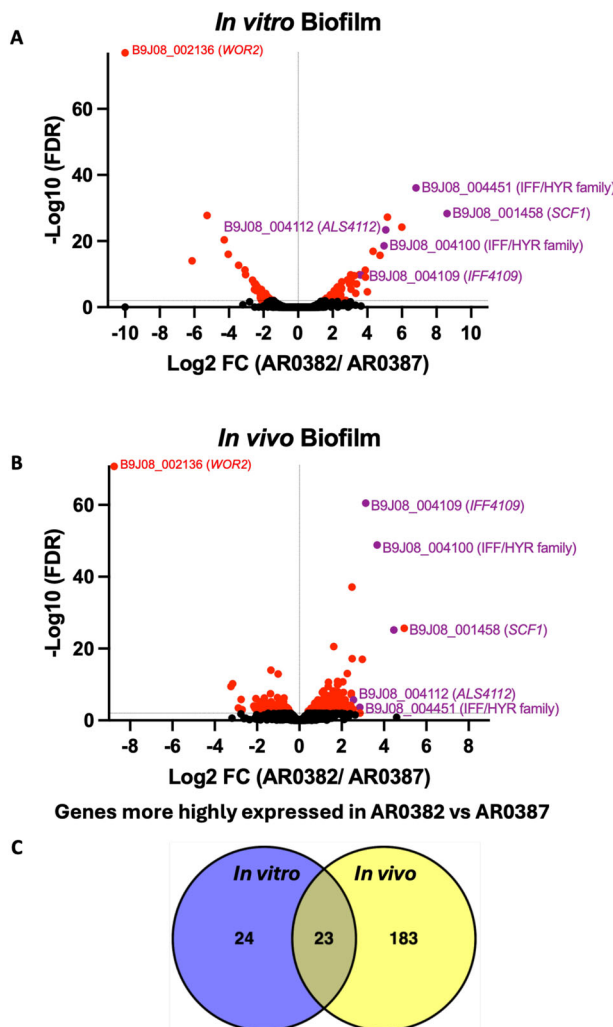


**Fig. 1 | RNA-seq analysis of in vitro and in vivo grown biofilms depicting genes differentially regulated in the aggregative *C. auris* strain AR0382 compared to the nonaggregative strain AR0387.** Volcano plots of comparative differential gene expressions during (A) in vitro and (B) in vivo biofilm growth. LFC, log (base 2) fold change. FDR false-discovery rate. Black: not statistically significant (FDR > 0.01). Red: Statistically significant (FDR < 0.01). Purple: Statistically significant and an adhesin. C Venn diagrams representing the overlap in the numbers of genes that are more highly expressed in strain AR0382 in vitro and in vivo.

### Confocal laser scanning microscopy (CLSM) and scanning electron microscopy (SEM) imaging reveal significant differences in biofilm architecture for *Δscf1* and *Δals4112* compared to the wild-type and *Δscf1+Δals4112* mixed biofilm

CLSM images revealed significant differences in the extent and structure of biofilms formed by the wild-type and *Δscf1*; where the wild-type biofilm consisted of dense matrix and cell aggregates, the *Δscf1* biofilm was patchy and less dense (Fig. 4). Although *Δals4112* formed a substantial biofilm, it was not as dense or aggregative as the wild-type. In contrast, biofilm formed by combination of *Δals4112* and *Δscf1* was comparable to that of the wild-type. SEM analysis revealed similar biofilm structures where wild-type and *Δals4112+Δscf1* mixed biofilms consisted of piles of cell aggregates, and biofilms of *Δals4112* and *Δscf1* were homogenous consisting mostly of single layer of cells (Fig. 5).

### Atomic force microscopy (AFM) reveals major differences in cell-cell adhesion forces between the different strains

Force-distance curves recorded by AFM<sup>32</sup> between two AR0382 wild-type cells featured a large adhesion force peak averaged at  $338 \pm 219$

pN (mean  $\pm$  standard deviation (SD),  $n = 1567$  adhesive curves from 6 cell combinations) (Fig. 6A, B). Moreover, some force profiles showed sawtooth patterns with multiple force peaks in the 200–500 pN range, which could be attributed to the sequential unfolding of the tandem repeat domains of Als proteins<sup>33</sup> (Fig. 2). Interestingly, a wide distribution of adhesion forces, composed of both weak and strong forces was observed for this strain. In the nonaggregative AR0387 strain however, intercellular adhesion was essentially non-existent (4%) and only weak forces of  $96 \pm 29$  pN (305 adhesive curves from 4 cell pairs) were measured (Fig. S1D–F). In contrast to AR0382, a significant decrease in adhesion frequency was observed for the *Δals4112* strain (from 80 to 30%) (Fig. 6C), where force curves featured only weak adhesion forces of  $127 \pm 27$  pN ( $n = 608$  adhesive curves from 6 cell pairs) (Fig. 6B), and sawtooth patterns were not observed (Fig. 6A). Similar intercellular adhesion forces were measured for the *Δscf1* strain ( $111 \pm 30$  pN,  $n = 731$  adhesive curves from 6 cell pairs), and an adhesion frequency slightly higher than what was observed for the *Δals4112* strain (46%) Fig. 6C). Finally, adhesion was also probed between cells of the *Δals4112* and *Δscf1* mutants; even though a mean adhesion frequency of 54% was registered (Fig. 6C), half of the cell pairs probed exhibited adhesion frequency in the same range of what was observed for the AR0382 wild-type strain. Despite this difference, intercellular adhesion forces of  $132 \pm 43$  pN ( $n = 1146$  adhesive curves from 8 cell combinations) were measured for the *Δals4112+Δscf1* experiment (Fig. 6A, B).

### SEM analysis of catheters implanted in mice showed impaired in vivo biofilm formation in *Δscf1* mutant compared to wild-type strains

SEM imaging of infected catheters recovered from mice (Fig. 7A) revealed significant differences in density and architecture of biofilms formed within the catheter lumens. The AR0382 wild-type strain formed a robust biofilm consisting of aggregates of cells; in contrast, biofilms within catheters infected with *Δscf1* were scarce with patches consisting primarily of extracellular matrix with fewer yeast cells in single layers and no or minimum cell aggregates, comparable to that formed by the nonaggregative AR0387 wild-type strain (Fig. 7B).

### Discussion

*Candida auris* avidly adheres and forms biofilms on indwelling medical devices such as intravascular catheters, an important risk factor for systemic infection. A striking morphological feature of some *C. auris* isolates is their capacity to aggregate and form strong biofilms<sup>18,27</sup>. In this study, we performed a comprehensive comparative analysis of biofilms formed by strains exhibiting a high and low aggregation phenotype under in vitro and in vivo growth conditions. First, our analysis focused on identifying genes that were more highly expressed in the aggregative strain both in vitro and in vivo, specifically those with predicted roles in adhesion and biofilm formation based on functional homology in other *Candida* species. Most notable among the genes that are more highly expressed in the aggregative strain were B9J08\_001458 and B9J08\_004112, which encode homologs of *C. albicans* *RBT1* and *ALSS*, respectively<sup>31,34,35</sup>. Recently, B9J08\_001458 was described as unique to *C. auris* and was named *SCF1* by Santana et al.<sup>28,36</sup>, protein domain analysis shows that both *Scf1* and *Saccharomyces cerevisiae* *Flo11p* share a N-terminal *Flo11* domain<sup>28</sup>. The *Flo* adhesin family initially discovered in brewer's yeast (*S. cerevisiae*) has the ability to form cellular aggregates induced by shear force<sup>18,29</sup>. Interestingly, we identified a *Flo11* domain in the *C. auris* *Scf1* and *C. albicans* *Rbt1* (Fig. 2). The *C. albicans* *Rbt1* adhesin is involved in cell-cell adhesion and overexpression of *RBT1* in *C. albicans* was shown to trigger the clustering of other cell surface proteins harboring aggregate-forming sequences such as *Hwp1*, by forming

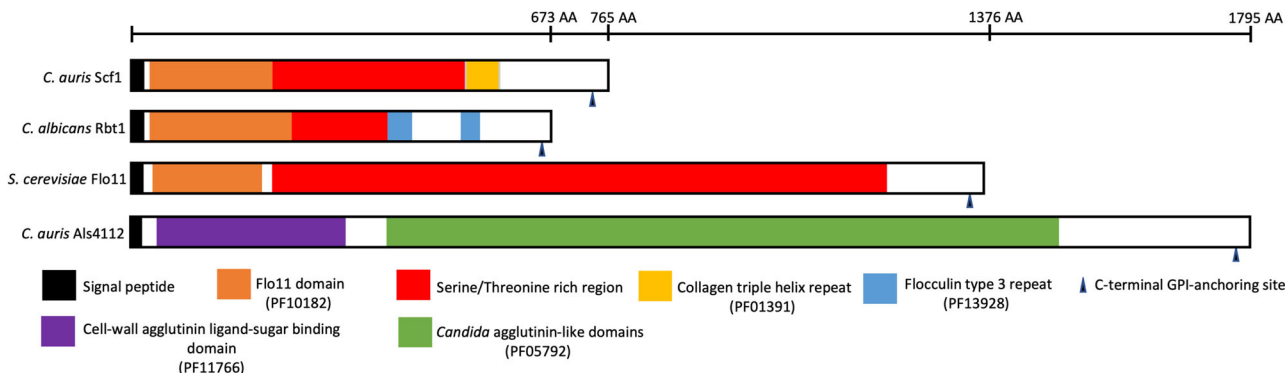


**Fig. 2 | Scf1 adhesin domain organization.** Diagram comparing the *C. auris* Scf1 domain structure to that of the *C. albicans* Rbt1 adhesin and the *Saccharomyces cerevisiae* Flo11 depicting a common Flo11 domain and a serine–threonine rich region (>50%) recognized by Als4112. Pfam database code is in parentheses; signal peptides and GPI-anchors were predicted using the prediction softwares SignalP

6.0 and NetGPI-1.1, respectively. Functional domains of adhesin proteins were identified via InterProScan (<https://www.ebi.ac.uk/interpro/search/sequence/>) (accessed February 12, 2024). Uniprot entries: AOA2H1A319 (Scf1); AOA8H6F4R1 (Rbt1); P08640 (Flo11); AOA2H0ZH9 (Als4112).

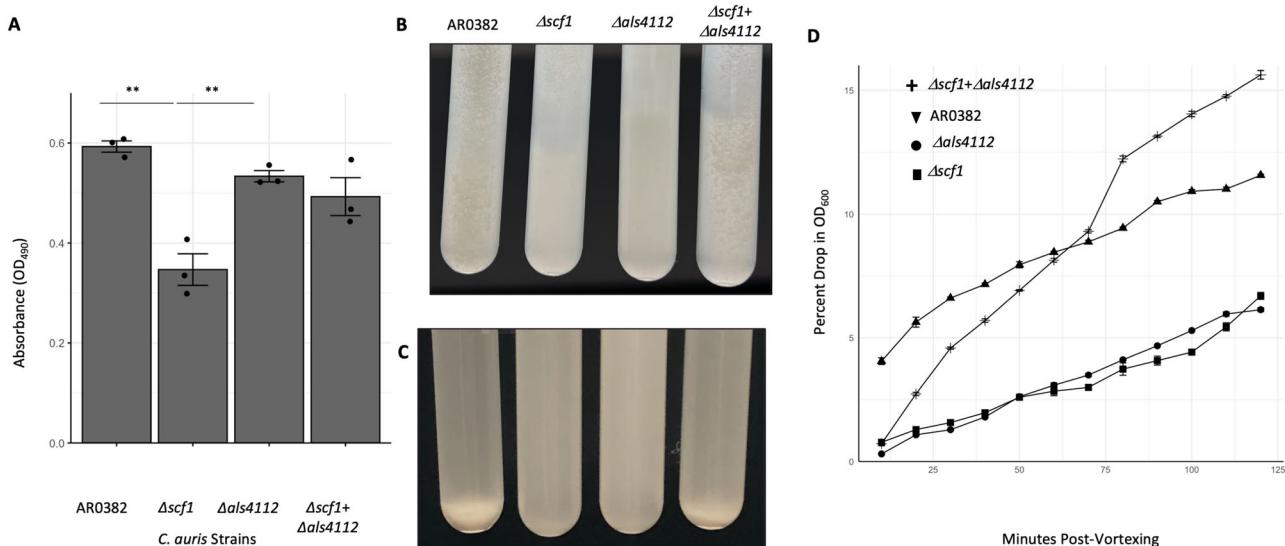


**Fig. 3 | Comparative evaluation of biofilm formation, aggregation, and sedimentation rate of  $\Delta$ scf1 and  $\Delta$ als4112 mutants individually and in combination compared to the wild-type (AR0382).** A Measurement of the metabolic activity of 24 h biofilms based on values of OD<sub>490</sub> comparing wild-type AR0382 to  $\Delta$ scf1 and  $\Delta$ als4112 mutants and  $\Delta$ scf1+ $\Delta$ als4112 combination. Statistical analysis was performed by one-way ANOVA and post hoc Tukey test with  $P$  values representing

significant differences. Bar plots show mean and standard error of mean of  $n=3$  biological replicates, each as an average of four technical replicates.  $P = 2.61 \times 10^{-3}$ ,  $1.75 \times 10^{-3}$ . B Cell aggregation 2 min after vigorous vortexing and C 10 min post-vortexing. D Measurement of rate of cell sedimentation over 2 h. Values represented are mean OD plus standard error of mean of three technical replicates. \*\* $0.001 < P \leq 0.01$ .

intermolecular bonds<sup>31,37</sup>. Further, Rbt1 is related to the Hwp1 and Hwp2 cell wall proteins that play distinct but overlapping roles in *C. albicans* for promoting biofilm formation<sup>38</sup>. In fact, the Hwp1 protein possesses an internal serine–threonine-rich region with a critical role in cell–cell adhesion and biofilm formation<sup>39</sup>. Therefore, we propose that Scf1 functions as an adhesin in a similar manner to the *C. albicans* Rbt1 and Hwp1.

Fungal cellular aggregation is proposed to occur as a result of a global cell surface conformational shift<sup>40</sup>. Therefore, we aimed to investigate the contribution of the *C. auris* Scf1 in relation to other expressed adhesins, primarily the co-upregulated Als4112. Heterologous expression of the *C. albicans* Als5 at the surface of *S. cerevisiae* was shown to result in Als5-mediated adhesion followed by the formation of multicellular aggregates, which was not observed when ALS5 was expressed at reduced levels<sup>41,42</sup>. In exploring the mechanism driving Als5-mediated intercellular adhesion, a study described an aggregation mechanism whereby amyloid core sequences in Als

proteins trigger the formation of cell surface adhesion nanoclusters, facilitating strong interactions between adhesins on opposing cells<sup>25</sup>. Interestingly, in *C. albicans*, Als5 adhesion was shown to be mediated by recognition of a minimum of four accessible contiguous threonine and serine residues<sup>43,44</sup>. Our analysis of the Scf1 protein sequence identified multiple patches of contiguous threonine and serine residues within a larger region of amino acids concentrated in serine–threonine residues, comparable to that in the *C. albicans* Hwp1 and Rbt1, further supporting the functional similarity of Scf1 to this class of *C. albicans* adhesins (Fig. 2). This degenerate “recognition system” among adhesins would provide *C. auris* with a plethora of target proteins for adherence<sup>44</sup>.

Interestingly, complementary roles for *C. albicans* Hwp1 and Als1/3 in biofilm formation have been described by Nobile et al.<sup>29</sup>, whereby a mixture of biofilm-defective *HWP1* and *ALS1/3* mutants could form a hybrid biofilm. Hence similarly, despite their sequence divergence, we posit that in *C. auris*, Als4112 and Scf1 may function redundantly to

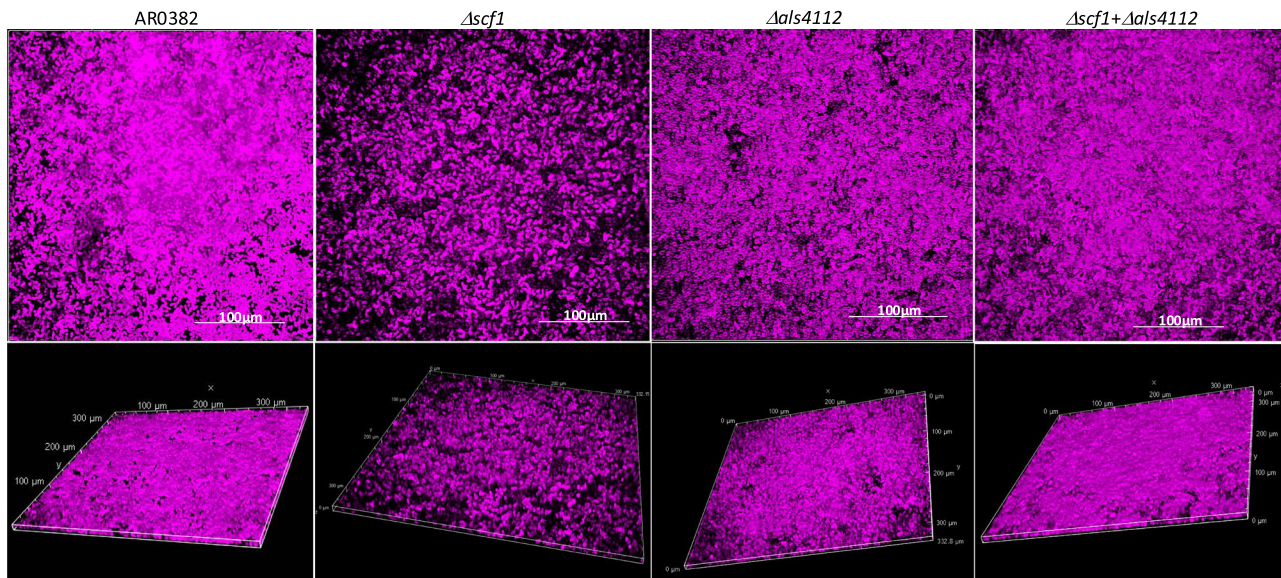


**Fig. 4 | Representative images from confocal laser scanning microscopy analysis of biofilms formed by the *C. auris* AR0382 wild-type (WT) strain and the  $\Delta scf1$  and  $\Delta als4112$  mutants grown individually and in combination**

**( $\Delta scf1+\Delta als4112$ )**. Z-stack reconstructions of biofilms stained with polysaccharide stain concanavalin A (fuchsia). Imaging was performed on at least 2 separate occasions.

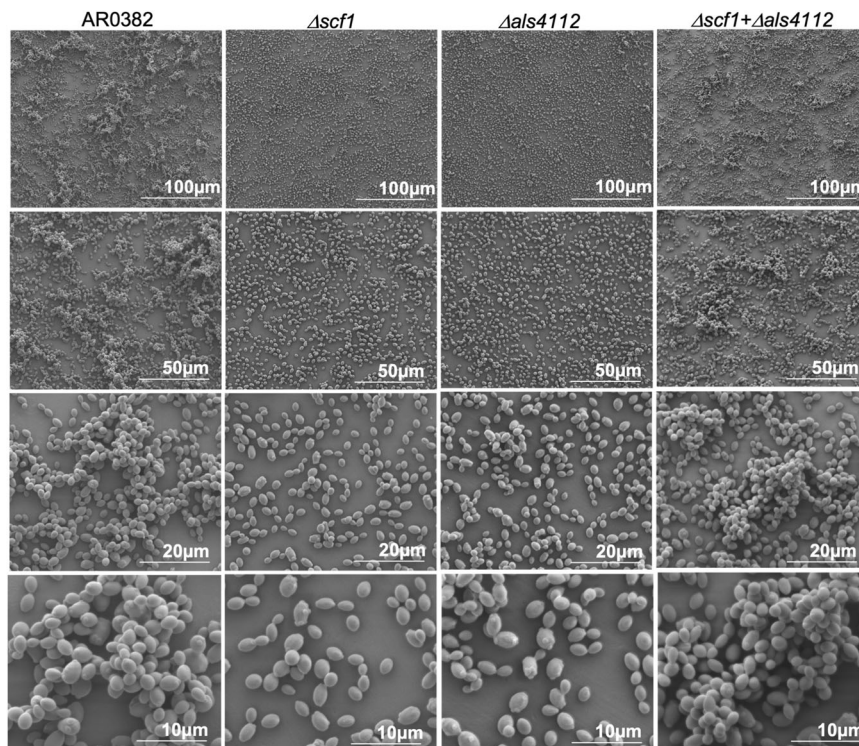


**Fig. 5 | Representative images from scanning electron microscopy analysis.** Twenty-four-hour biofilms formed by the *C. auris* AR0382 wild-type (WT) strain and the  $\Delta scf1$  and  $\Delta als4112$  mutants grown individually and in combination ( $\Delta scf1+\Delta als4112$ ). Imaging was performed on at least two separate occasions.

promote cell–cell interaction and biofilm formation (Fig. 8). To that end, we generated gene deletion strains of *C. auris* *SCF1* and *ALS4112* in the aggregative strain AR0382. Interestingly, phenotypic evaluations demonstrated reduced adhesion and biofilm formation in vitro for the  $\Delta scf1$  mutant, but not for the  $\Delta als4112$  mutant compared to the wild-type strain (Fig. 3A). Individually, cells of  $\Delta scf1$  and  $\Delta als4112$  lost aggregation capability, but aggregation was restored when combined (Fig. 3B–D). This aggregation was also demonstrated by SEM analysis,

revealing a confluent mixed biofilm comprised of heaps of co-adhering cells, comparable to that seen with the wild-type (Fig. 5). Interestingly, however, although based on assessment of metabolic activity the  $\Delta als5$  biofilm was comparable to that of the wild-type, SEM biofilm imaging revealed dramatic structural differences. These observations corroborate a previous report that *Als4112* is not crucial for adherence to abiotic surfaces<sup>28</sup>. However, here we show that this adhesin is necessary for mediating cell–cell adherence. Due to the observed reduction

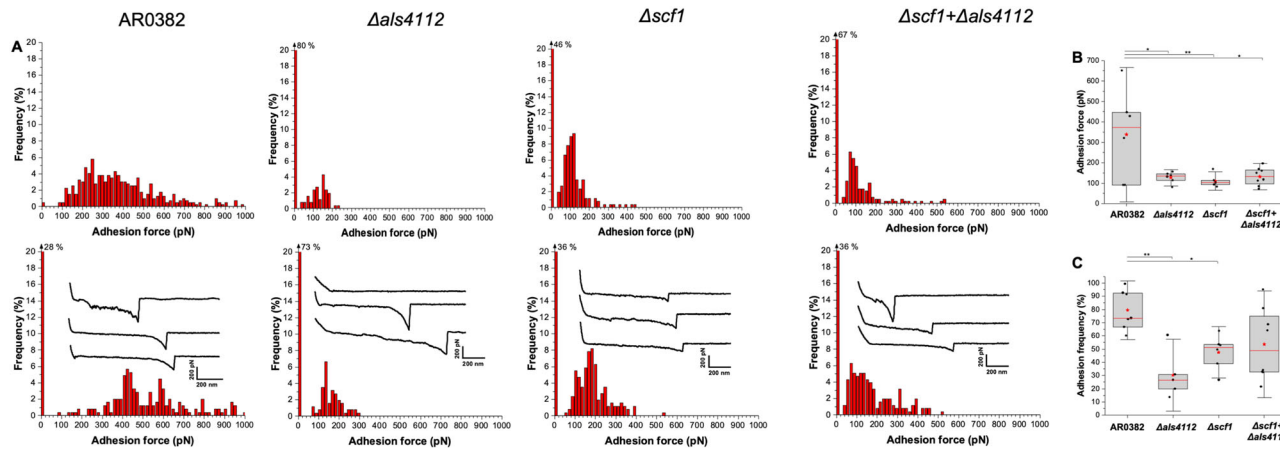


**Fig. 6 | Single-cell force spectroscopy of *C. auris* cell–cell adhesion.** **A** Adhesion force histograms with representative retraction profiles (inset) obtained for the interaction between AR0382 wild-type cells, cells of  $\Delta\text{als4112}$ , cells of  $\Delta\text{scf1}$  and between cells of  $\Delta\text{als4112}$  and  $\Delta\text{scf1}$  ( $\Delta\text{als4112} + \Delta\text{scf1}$ ); 2 representative cell pairs are shown for each strain. **B** Adhesion force boxplots show data on  $n = 6$  pairs of AR0382 cells,  $n = 5$  pairs of  $\Delta\text{als4112}$  cells,  $n = 6$  pairs of  $\Delta\text{scf1}$  cells and  $n = 8$  pairs between  $\Delta\text{als4112} + \Delta\text{scf1}$  cells.  $P = 1.71 \times 10^{-3}$ ,  $3.77 \times 10^{-2}$ . Red stars represent the mean values, red lines are the medians, boxes are the 25–75% quartiles and whiskers the standard deviation from mean. \* $0.01 < P \leq 0.05$ , \*\* $0.001 < P \leq 0.01$ . Statistical analysis was performed by one-way ANOVA and post hoc

Tukey test with  $P$  values representing significant differences.  $P = 1.42 \times 10^{-2}$ ,  $7.69 \times 10^{-3}$ ,  $1.01 \times 10^{-2}$ . **C** As in (B), adhesion frequency boxplots show data on  $n = 7$  pairs of AR0382 cells,  $n = 5$  pairs of  $\Delta\text{als4112}$  cells,  $n = 6$  pairs of  $\Delta\text{scf1}$  cells and  $n = 8$  pairs between  $\Delta\text{als4112} + \Delta\text{scf1}$  cells.  $P = 1.71 \times 10^{-3}$ ,  $3.77 \times 10^{-2}$ . Red stars represent the mean values, red lines are the medians, boxes are the 25–75% quartiles and whiskers the standard deviation from mean. \* $0.01 < P \leq 0.05$ , \*\* $0.001 < P \leq 0.01$ .

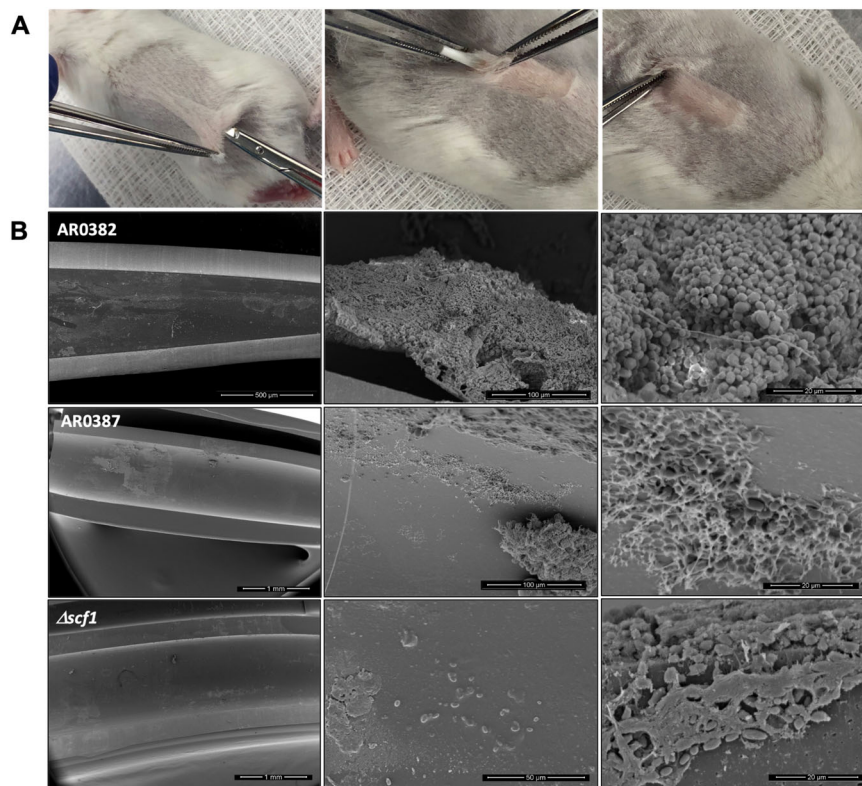


**Fig. 7 | Infection and biofilm formation in catheters implanted in mice.** **A** A small incision is made in a shaved area in the dorsum of anesthetized mice and catheter fragments (0.5 cm) are inserted within a formed subcutaneous tunnel. **B** Scanning electron microscopy of explanted catheters. Representative low- and high-

magnification SEM images demonstrating mature biofilm formed within lumen of catheters infected with AR0382 wild-type strain consisting of aggregates of yeast cells. Imaging was performed on at least two separate occasions.

in the ability of  $\Delta\text{scf1}$  to form biofilm in vitro, we then tested this mutant in our mouse model to evaluate biofilm formation in vivo. In contrast to the dense aggregative biofilm formed by the AR0382 strain, SEM imaging of the biofilms within catheters revealed a minimal biofilm formed by  $\Delta\text{scf1}$ , comparable to that of the AR0387 strain consisting primarily of single layers of yeast cells (Fig. 7).

The strong cell–cell affinities between the  $\Delta\text{scf1}$  and  $\Delta\text{als4112}$  mutants were assessed by measuring adhesion forces using single-cell force spectroscopy (Fig. 6). With the wild-type strain, a wide distribution of adhesion forces composed of both weak and strong forces were detected, indicative of a complex binding mechanism that involves a combination of single and multiple molecular bonds. The involvement

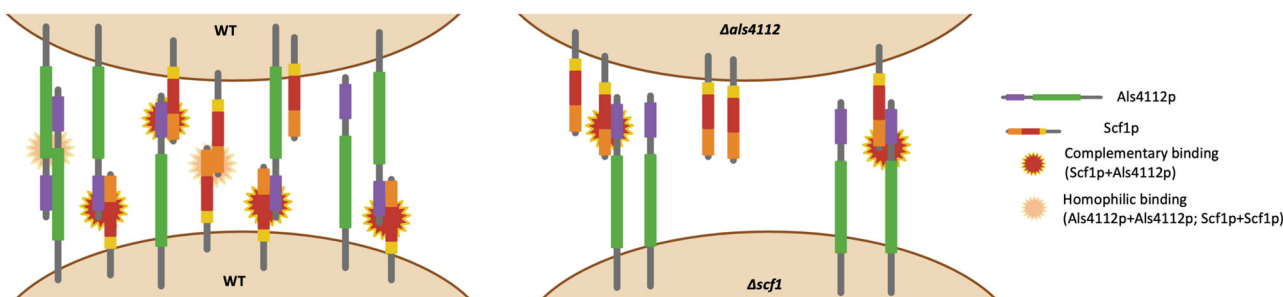


**Fig. 8 | Hypothetical mechanistic model depicting complementary Scf1/Als4112 binding.** (left) Adherence between wild-type (WT) cells involving Scf1+Als4112 and complementary binding and homophilic interactions between Als4112+Als4112 and

Scf1+Scf1; (right) Complementary binding between Scf1 and Als4112 on the  $\Delta$ als4112 and  $\Delta$ scf1 mutant cells, respectively. Domain designations and colors are consistent with those in Fig. 2.

of the Als4112 and Scf1 adhesin in cell–cell adhesion was demonstrated by the significant decrease in adhesion frequency observed between cells of the  $\Delta$ als4112 and  $\Delta$ scf1 strain, which was partially restored by mixing the two deletion strains. High forces were not completely restored however when probing  $\Delta$ als4112 cells with  $\Delta$ scf1 cells (and vice versa), indicating that *C. auris* cell–cell adhesion not only involves a combination of single and multiple Als4112-Scf1 bonds, but also Als4112-Als4112 and Scf1-Scf1 homophilic bonds, and potentially other mechanisms (Fig. 8). In fact, it is well-documented for *C. albicans* that Als5 proteins are able to form intercellular amyloid bonds through their T domains to promote biofilm formation<sup>25,33,45,46</sup>. In addition, since the *C. albicans* Rbt1 was also shown to be capable of forming amyloid bonds<sup>37,47</sup>, it is tempting to speculate that similar homophilic binding might similarly occur with the *C. auris* Scf1 adhesin. Combined, these findings indicate that Als4112 and Scf1 undergo a complementary heterophilic binding reaction that supports *C. auris* cell–cell adherence, critical for intraspecies adhesin interactions and promoting formation of monospecies biofilms.

Collectively, our findings demonstrated significant in vitro and in vivo transcriptional changes associated with the *C. auris* aggregative form impacting cell wall adhesins that although with little similarity, may have complementary roles, and function redundantly to promote cell–cell interaction and biofilm formation (Fig. 8). Functional diversity of cell wall proteins may be a form of regulation providing the *C. auris* aggregative phenotype with flexibility and rapid adaptation to the environment, potentially impacting persistence and virulence.

## Methods

### Ethics statement

All animal experiments were conducted at the AAALAC-accredited Animal Facility of the University of Maryland, Baltimore and were approved by Animal Care and Use Committee, in compliance with National Institutes of Health standards under protocol AUP-00000005. Sex was not considered in the study design and analysis. The model was established and standardized using female mice and used in our previous studies.

### Strains and growth conditions

The *C. auris* wild-type strains AR0382 (B1109) and AR0387 (B8441) from the CDC AR-panel were used as wild-type strains in this study. We have previously characterized these strains and designated AR0382 as aggregative/high biofilm former and AR0387 as non-aggregative/low biofilm former<sup>16</sup>. Both isolates were confirmed to belong to clade I (South Asian) based on ref. 48 and were isolated in Pakistan; AR0382 was recovered from a burn wound and AR0387 from blood. Mutant strains of *C. auris* genes B9J08\_001458 and B9J08\_004112 in the AR0387 and AR0382 backgrounds were generated in this study. These genes have since been named SCF1 and ALS4112, respectively<sup>27,28</sup>. Isolates were grown overnight in yeast

peptone dextrose broth (YPD) (Difco Laboratories) at 30 °C, washed in phosphate-buffered saline (PBS) and resuspended in PBS to the final cell density needed.

### In vitro transcriptional analysis of AR0387 and AR0382 biofilms using RNA-sequencing

Biofilms of both wild-type strains were formed in 6-well plates in RPMI 1640-HEPES media (Invitrogen) at 37 °C for 24 h. Following incubation, wells were rinsed with PBS and biofilms were scraped. Recovered cells were snap-frozen on dry ice and ethanol, allowed to thaw at room temperature (RT), then incubated for 30 min at 37 °C in “digestion buffer” containing 100 U/ml of lyticase and RNase inhibitor in TRIS-EDTA 1× buffer. RNA was extracted in 1 ml of TRI Reagent™ Solution (Ambion, Invitrogen; Carlsbad, CA) using bead-beating for 30 min at RT followed by purification using Direct-zol RNA Miniprep kit (Zymo Research; Tustin, CA). Eluted RNA was analyzed in a Nanodrop Lite (Thermo Scientific). Total RNA was subjected to rRNA depletion with the Ribominus Eukaryote Kit. All RNA-seq libraries (strand-specific, paired-end) were prepared with the TruSeq RNA sample prep kit (Illumina). One hundred nucleotides of the sequence were determined from both ends of each cDNA fragment using the Novaseq platform (Illumina). Sequencing reads were aligned to the reference genomes (*C. auris* strain B8441) using HISAT2<sup>49</sup>, and alignment files were used to generate read counts for each gene; statistical analysis of differential gene expression was performed using the DEseq package from Bioconductor<sup>50</sup>. A gene was considered differentially expressed if the absolute log fold change was greater than or equal to 1 and the FDR value for differential expression was below 0.01. The RNA-seq analysis was performed in biological triplicate. Given the limited annotation of the *C. auris* genome, some of the gene names reported are based on homology to *C. albicans* genes. For genes with no recognizable orthologs, the original systematic *C. auris* gene designation is provided.

### In vivo transcriptional analysis of AR0387 and AR0382 biofilms formed within catheters implanted in mice using RNA sequencing

Three-month-old female Balb/c mice (Jackson Laboratory) were housed at a maximum of five per cage, weighed and closely monitored for any signs of distress. A modified model previously described by Kucharíková et al.<sup>51</sup> was used; 0.5 cm fragments of polyurethane triple-lumen central venous catheters (Jorgensen Laboratories) pre-coated overnight with fetal bovine serum (Gibco™) were incubated with  $1 \times 10^8$  cells/ml cell suspensions in PBS for 1.5 h at 37 °C, rinsed and kept on ice until implanted. For each experimental set, in vitro-infected catheters were processed for assessment of microbial recovery. Mice were anesthetized with 0.5 ml intraperitoneal injections of tribromoethanol (TBE) solution (250 mg/kg; Sigma-Aldrich); the dorsum of mice was shaved and a small incision made aseptically, and a subcutaneous

tunnel was created allowing for insertion of up to five pieces of pre-inoculated catheters (Fig. 7A). Incisions were sealed using 3 M Vetbond™ tissue glue and lidocaine analgesic gel was applied. Biofilms were allowed to form within catheters for 72 h then animals were euthanized by CO<sub>2</sub> inhalation followed by cervical dislocation. Catheters were collected in RNAlater buffer, aseptically fragmented, sonicated in RNase-free water and cells from all catheters recovered from each mouse were pooled by centrifugation. RNA sequencing was performed as described above. The AR0382 group contained three biological replicates and the AR0387 group contained four biological replicates. A total of 40 mice were used.

### Generation of mutant strains of genes B9J08\_001458 (*SCF1*) and B9J08\_004112 (*ALS4112*)

All primers used are provided in Supplementary Table 1. *Plasmid construction:* The plasmids used in this study were propagated in *E. coli* TOP10F' chemically competent cells. Bacterial transformations were carried out by heat shock at 42 °C for 45 s using 30 µl of competent cells, and subsequent cooling on ice for 2 min. The transformants were selected on solid LB (Sigma, Fisher Scientific) medium (agar 15%, Bacto™ Agar, BD) supplemented with ampicillin (100 µg/ml). To construct the deletion mutants, we utilized the SAT1 flipper tool<sup>52</sup>. Specifically, the upstream and downstream regions of the genes of interest were amplified from the genomic DNA of *C. auris* strain B8441 and cloned into pSFS2 in a homodirectional way so that they flanked the nourseothricin resistance marker (*SAT1*) and the *FLP* recombinase gene. To generate the B9J08\_001458 deletion cassette, the upstream homologous region was cloned into the Xhol/KpnI-HF (NEB) digested pSFS2 plasmid using NEBuilder HiFi (NEB) as per manufacturer instructions. The resulting constructs were isolated from the transformants, digested with SacI-HF and NotI-HF and the downstream region was cloned into the digested plasmid. To generate the B9J08\_004112 deletion cassette, the upstream homologous region was cloned into the Apal/KpnI-HF (NEB) digested pSFS2 plasmid. Resulting constructs were isolated from the transformants, digested with SacII and NotI-HF and the downstream region was cloned into the digested plasmid. All inserts of the plasmids were verified by sequencing (Mix2Seq, Eurofins genomics). To produce a linear deletion cassette, each plasmid was digested with KpnI-HF and SacII for the B9J08\_004112 deletion cassette and with StuI and Scal for the B9J08\_001458 deletion cassette.

*Strain construction:* For strain construction, *C. auris* cells were prepared as described by Carolus et al.<sup>53</sup>. For electroporation, 40 µl of competent cells was mixed with the transformation mixture and transferred to 2 mm electroporation cuvettes (Pulsestar, Westburg). The transformation mixtures comprised 3 µl of 4 µM Alt-R™ S.p. Cas9 Nuclease V3, 3.6 µl of duplexed gene-specific Alt-R® CRISPR-Cas9 crRNA (IDT) with Alt-R® CRISPR-Cas9 tracrRNA (IDT) and 500 ng of the linearized constructed pSFS2 variant for each gene as donor DNA. A single pulse was given at 1.8 kV, 200 W, 25 mF, and the transformation mixture was immediately transferred to 2 ml YPD in test tubes and incubated for 4 h at 37 °C at 150 rpm. Cells were collected by centrifugation for 5 min at 5000×g, resuspended in 100 µl YPD and plated on YPD agar containing 200 µg/ml of nourseothricin (Jena Bioscience). The sequences of the crRNA are provided in Supplementary Data. Correct transformants were screened by colony PCRs, using the Taq DNA Polymerase (NEB) and primers that bind in the deletion cassette and outside of the homologous regions upstream and downstream. Null mutants of B9J08\_001458 (*SCF1*) and B9J08\_004112 (*ALS4112*) were generated in triplicate (3 independent transformants; Δ1-Δ3) in both wild-type backgrounds (AR0387 and AR0382) and evaluated for biofilm formation but only one representative mutant was randomly selected for subsequent analysis (Fig. S3).

For the reintroduction of B9J08\_001458 (*SCF1*) and B9J08\_004112 (*ALS4112*) in the AR0382 background, one biological replicate of each

deletion strain was used. The deletion mutants were grown in YPD and plated out until they lost the nourseothricin resistance marker. The excision of the deletion cassette was verified by PCR. The FRT scar was then targeted by using the pJM19 vector as per the protocol described in ref. 53. The episomal plasmid CRISPR method allowed for a scarless reintegration of each gene without introducing any trans elements to the genomic DNA of the mutants. The genomic regions of B9J08\_001458 and B9J08\_004112, including 500 bp upstream and downstream were amplified from the genome of AR0382 and used as the donor DNA. The transformants were selected on YPD (nourseothricin 200 µg/ml) and screened using primers binding outside of the homologous regions and in the ORF sequence. To ensure proper integration both upstream and downstream junctions were checked by PCR and subsequently by target sequencing (Eurofins Genomics, TubeSeq).

### Evaluation of potential complementary roles for the *Scf1* and *Als4112* adhesins in surface adhesion and biofilm formation

To determine the impact of gene deletions on adherence and biofilm formation and whether there are adherence complementary roles for the *Scf1* and *Als4112* adhesins, mutant strains were compared to the wild-type strain individually and in combination in biofilm assays based on assessment of metabolic activity. Biofilms were grown by seeding 200 µl of 1 × 10<sup>6</sup> cells/ml cell suspensions of each strain in flat-bottom 96-well polystyrene microtiter plates; for combination biofilms, mixed solutions of 100 µl of 1 × 10<sup>6</sup> cells/ml cell suspensions of each mutant were used. Following incubation at 37 °C for 24 h, wells were washed with PBS and biofilms evaluated using the MTS metabolic assay (Promega) as per the manufacturer recommendation. Color intensity was measured at 490 nm using a Cell Imaging Multi-Mode Reader (Cytation 5, Biotek). Assays were performed on three separate occasions, each using four technical replicates.

### Evaluation of potential complementary roles for the *Scf1* and *Als4112* adhesins in cell-cell adherence and coaggregation

The contribution of adhesins to cell-cell interaction and coaggregation was comparatively assessed based on formation of cell aggregates. For coaggregation assays, cell suspensions of wild-type strain and mutant strains were suspended in PBS to final density of 5 × 10<sup>8</sup> cells/ml in 5-ml plastic tubes, and suspensions vigorously vortexed for 1 min. To evaluate adherence complementation of adhesins, suspensions of both mutants at 2.5 × 10<sup>8</sup> cells/ml were equally mixed and vortexed. Tubes were placed upright at RT and cell aggregation was monitored and imaged. In addition, sedimentation rate of formed cell aggregates was also measured based on drop in absorbance readings of cell suspensions. For these experiments, aliquots from cell suspensions were measured at 600 nm every 10 min for up to 2 h in a BioTek 800 TS absorbance reader. The sedimentation rate was calculated as the percent reduction in absorbance at each time-point compared to the initial reading.

### Confocal laser scanning microscopy (CLSM) and scanning electron microscopy (SEM) analysis of biofilms of wild-type and the *Δscf1* and *Δals4112* mutants grown individually and in combination

For CLSM, biofilms of wild-type and mutant strains individually and in combination were grown on glass coverslip-bottom dishes (MatTek Co., Ashland, MA) for 24 h; biofilms were rinsed in PBS and then stained with a concanavalin A conjugated to Alexa 647 (Invitrogen) (50 µg/ml) for 45 min at 37 °C. Biofilms were visualized using an inverted confocal laser scanning microscope (T2i, Nikon) and images analyzed using Imaris 9.3 Arena software and ImageJ. For SEM, biofilms were grown on coverslips for 24 h at 37 °C then fixed in 2%

paraformaldehyde-2.5% glutaraldehyde, post-fixed with 1% osmium tetroxide, serially dehydrated in ethyl alcohol (30–100%) and critical-point dried. Samples were carbon-coated and observed with Quanta 200 SEM (FEI Co.) and images processed using Adobe Photoshop software.

### In vivo evaluation of AR0382 and AR0387 wild-type strains and $\Delta scf1$ mutant in a mouse subcutaneous catheter model

Based on observed in vitro biofilm deficiency of the  $\Delta scf1$  mutant, its ability to form biofilm on catheters in vivo was evaluated in the subcutaneous catheter model. For these experiments, 3-month-old female Balb/c mice were used. The adherence of  $\Delta scf1$  was compared to both the aggregative (AR0382) and nonaggregative (AR0387) wild-type strains. For these experiments, catheter fragments inoculated with the strains in vitro were implanted in animals as described above. Biofilms were allowed to form within catheters for 72 h then animals were euthanized and catheters harvested. To visualize the biofilms formed within the catheter lumen, catheters from each group were cut longitudinally to expose the lumen, fixed, and processed for SEM analysis as described above. Catheters from six mice were analyzed, and representative images were presented.

### Comparative evaluation of cell–cell adhesion forces between cells of *C. auris* strains using single-cell force spectroscopy (SCFS)

SCFS was employed to measure single cell–cell adhesion forces among cells of wild-type and the two mutants<sup>32,54,55</sup>. For these studies, a single live cell was attached to a polydopamine-coated tipless AFM cantilever and approached toward another single cell, previously immobilized on a dish. The retraction and approach movement of the cell probe was monitored and force–distance curves recorded, allowing quantification of the forces driving intercellular adhesion. Triangular tipless cantilevers (NP O10, Bruker) were immersed for 1 h in Tris-buffered saline solution (50 mM Tris, 150 mM NaCl, pH 8.5) containing 4 mg/ml of dopamine hydrochloride, rinsed with Tris-buffered saline solution and mounted on the AFM setup for cell probe preparation. Calibration of the probe was performed prior to the AFM experiment and its nominal spring constant determined by the thermal noise method. *C. auris* cells were grown overnight in liquid YPD at 37 °C, 150 rpm, harvested by centrifugation, washed three times in 1× PBS and finally diluted 1000-fold. Cell suspensions were allowed to adhere to polystyrene dishes for 20 min and dishes washed three times then filled with 2 ml of 1× PBS before being transferred to the AFM setup. SCFS measurements were performed at RT in 1× PBS, using a Nanowizard 4 AFM (JPK Instrument, Berlin, Germany). The cell probe was prepared by bringing the polydopamine-coated cantilever into contact with an isolated cell and, once the probe was retracted, its attachment to the cantilever was confirmed using an inverted optical microscope. The cell probe was then positioned over an immobilized cell and force maps of 16 × 16 pixels were recorded on top of it, using a contact force setpoint of 250 pN, a constant approach and retraction speeds of 1 μm/s and an additional pause at contact of 1 s. Adhesion forces were extracted from force–distance retraction curves by considering the rupture event for which the adhesion force was maximal, for every curve.

### Data analysis

Statistical analysis of biofilm growth was performed using R statistical programming software. Statistical analysis of SCFS data was performed with Origin software (OriginPro 2021). To compare differences among strains in in vitro biofilm-forming capabilities and cell–cell adhesion force and frequency, a one-way ANOVA with Tukey's post hoc test was used. *P* values less than 0.05 were considered significant. Two-tailed Welch's *t* tests were used to compare absorbance values,

adhesion force and adhesion frequency between AR0382 and AR0387 strains. Ggplot2 and ggpubr packages were used to construct models for figure construction.

### Reporting summary

Further information on research design is available in the Nature Portfolio Reporting Summary linked to this article.

### Data availability

All of the raw sequencing reads from this study are available at the NCBI Sequence Read Archive (SRA) under BioProject accession number PRJNA1086003. All strains generated in this study will be made available upon request from authors. Source data are provided with this paper.

### References

- Vila, T., Sultan, A. S., Montelongo-Jauregui, D. & Jabra-Rizk, M. A. *Candida auris*: a fungus with identity crisis. *Pathog. Dis.* **78**, ftaa034 (2020).
- Lockhart, S. R. et al. Simultaneous emergence of multidrug-resistant *Candida auris* on 3 continents confirmed by whole-genome sequencing and epidemiological analyses. *Clin. Infect. Dis.* **64**, 134–140 (2017).
- Cortegiani, A., Misseri, G., Giarratano, A., Bassetti, M. & Eyre, D. The global challenge of *Candida auris* in the intensive care unit. *Crit. Care Med.* **23**, 150 (2019).
- Lyman, M. et al. Worsening spread of *Candida auris* in the United States, 2019 to 2021. *Ann. Intern. Med.* **176**, 489–495 (2023).
- de Jong, A. W. & Hagen, F. Attack, defend and persist: how the fungal pathogen *Candida auris* was able to emerge globally in healthcare environments. *Mycopathologia* **148**, 353–365 (2019).
- Wickes, B. L. Analysis of a *Candida auris* outbreak provides new insights into an emerging pathogen. *J. Clin. Microbiol.* **58**, e02083–19 (2020).
- Lockhart, S. R. *Candida auris* and multidrug resistance: defining the new normal. *Fungal Genet. Biol.* **131**, 103243 (2019).
- Chaabane, F., Graf, A., Jequier, L. & Coste, A. T. Review on antifungal resistance mechanisms in the emerging pathogen *Candida auris*. *Front Microbiol.* **10**, 2788 (2019).
- Carolus, H. et al. Genome wide analysis of experimentally evolved *Candida auris* reveals multiple novel mechanisms of multidrug resistance. *mBio* **12**, e03333–03320 (2021).
- Horton, M. V., Holt, A. M. & Nett, J. E. Mechanisms of pathogenicity for the emerging fungus *Candida auris*. *PLoS Pathog.* **19**, e1011843 (2023).
- Fisher, M. C. et al. Tackling the emerging threat of antifungal resistance to human health. *Nat. Rev. Microbiol.* **20**, 557–571 (2022).
- Harris, E. *Candida auris* fungal infections and drug resistance on the rise. *JAMA* **329**, 1248 (2023).
- Fisher, M. C. & Denning, D. W. The WHO fungal priority pathogens list as a game-changer. *Nat. Rev. Microbiol.* **21**, 211–212 (2023).
- Larkin, E. et al. The emerging pathogen *Candida auris*: Growth phenotype, virulence factors, activity of antifungals, and effect of SCY-078 on growth morphology and biofilm formation., a novel glucan synthesis inhibitor. *Antimicrob. Agents Chemother.* **61**, e02396–02316 (2017).
- Sherry, L. et al. Biofilm-forming capability of highly virulent, multidrug-resistant *Candida auris*. *Emerg. Infect. Dis.* **23**, 328–331 (2017).
- Vila, T. et al. Comparative evaluations of the pathogenesis of *Candida auris* phenotypes and *Candida albicans* using clinically relevant murine models of infections. *mSphere* **5**, e00760–20 (2020).
- Kean, R. et al. Transcriptome assembly and profiling of *Candida auris* reveals novel insights into biofilm-mediated resistance. *mSphere* **3**, e00334–00318 (2018).

18. Willaert, R. G., Kayacan, Y. & Devreese, B. The Flo adhesin family. *Pathogens* **10**, 1397 (2021).
19. Dominguez, E. G. et al. Conserved role for biofilm matrix polysaccharides in *Candida auris* drug resistance. *mSphere* **4**, e00680-00618 (2019).
20. Brown, J. L. et al. *Candida auris* phenotypic heterogeneity determines pathogenicity in vitro. *mSphere* **5**, e00371-00320 (2020).
21. Short, B. et al. *Candida auris* exhibits resilient biofilm characteristics in vitro: implications for environmental persistence. *J. Hosp. Infect.* **103**, 92–96 (2019).
22. Szekely, A., Borman, A. M. & Johnson, E. M. *Candida auris* isolates of the southern Asian and South African lineages exhibit different phenotypic and antifungal susceptibility profiles in vitro. *J. Clin. Microbiol.* **57**, 1–12 (2019).
23. de Groot, P. W., Bader, O., de Boer, A. D., Weig, M. & Chauhan, N. Adhesins in human fungal pathogens: glue with plenty of stick. *Eukaryot. Cell* **12**, 470–481 (2013).
24. Sundstrom, P. Adhesion in *Candida* spp. *Cell Microbiol.* **4**, 461–469 (2002).
25. Dehullu, J. et al. Fluidic force microscopy demonstrates that homophilic adhesion by *Candida albicans* Als proteins is mediated by amyloid bonds between cells. *Nano Lett.* **19**, 3846–3853 (2019).
26. Malavia-Jones, D. et al. Strain and temperature dependent aggregation of *Candida auris* is attenuated by inhibition of surface amyloid proteins. *Cell Surf.* **10**, 100110 (2023).
27. Bing, J. et al. Clinical isolates of *Candida auris* with enhanced adherence and biofilm formation due to genomic amplification of ALS4. *PLoS Pathog.* **19**, e1011239 (2023).
28. Santana, D. J. et al. A *Candida auris*-specific adhesin, Scf1, governs surface association, colonization, and virulence. *Science* **381**, 1461–1467 (2023).
29. Nobile, C. J. et al. Complementary adhesin function in *C. albicans* biofilm formation. *Curr. Biol.* **18**, 1017–1024 (2008).
30. Soll, D. R. The role of phenotypic switching in the basic biology and pathogenesis of *Candida albicans*. *J. Oral Microbiol.* **6**, 22993 (2014).
31. Kim, S. H. et al. Genetic analysis of *Candida auris* implicates Hsp90 in morphogenesis and azole tolerance and Cdr1 in azole resistance. *mBio* **10**, e02529–02518 (2019).
32. Viljoen, A. et al. Force spectroscopy of single cells using atomic force microscopy. *Nat. Rev. Methods Prim.* **1**, 64 (2021).
33. Alsteens, D., Garcia, M. C., Lipke, P. N. & Dufrêne, Y. F. Force-induced formation and propagation of adhesion nanodomains in living fungal cells. *Proc. Natl. Acad. Sci. USA* **107**, 20744–20749 (2010).
34. Skrzypek, M. S. et al. The *Candida* Genome Database (CGD): incorporation of assembly 22, systematic identifiers and visualization of high throughput sequencing data. *Nucleic Acids Res.* **45**, D592–D596 (2017).
35. Muñoz, J. F. et al. Clade-specific chromosomal rearrangements and loss of subtelomeric adhesins in *Candida auris*. *Genetics* **218**, iyab029 (2021).
36. Balakumar, A., Bernstein, D. & Thangamani, S. The adhesin SCF1 mediates *Candida auris* colonization. *Trends Microbiol.* **32**, 4–5 (2024).
37. Monniot, C. et al. Rbt1 protein domains analysis in *Candida albicans* brings insights into hyphal surface modifications and Rbt1 potential role during adhesion and biofilm formation. *PLoS ONE* **8**, e82395 (2013).
38. Ene, I. V. & Bennett, R. J. Hwp1 and related adhesins contribute to both mating and biofilm formation in *Candida albicans*. *Eukaryot. Cell* **8**, 1909–1913 (2009).
39. Nobile, C. J., Nett, J. E., Andes, D. R. & Mitchell, A. P. Function of *Candida albicans* adhesin Hwp1 in biofilm formation. *Eukaryot. Cell* **5**, 1604–1610 (2006).
40. Rauceo, J. M. et al. Global cell surface conformational shift mediated by a *Candida albicans* adhesin. *Infect. Immun.* **72**, 4948–4955 (2004).
41. Hoyer, L. L., Green, C. B., Oh, S. H. & Zhao, X. Discovering the secrets of the *Candida albicans* agglutinin-like sequence (ALS) gene family—a sticky pursuit. *Med. Mycol.* **46**, 1–15 (2008).
42. Gaur, N. K., Klotz, S. A. & Henderson, R. L. Overexpression of the *Candida albicans* ALA1 gene in *Saccharomyces cerevisiae* results in aggregation following attachment of yeast cells to extracellular matrix proteins, adherence properties similar to those of *Candida albicans*. *Infect. Immun.* **67**, 6040–6047 (1999).
43. Gaur, N. K., Smith, R. L. & Klotz, S. A. *Candida albicans* and *Saccharomyces cerevisiae* expressing ALA1/ALS5 adhere to accessible threonine, serine, or alanine patches. *Cell Commun. Adhes.* **9**, 45–57 (2002).
44. Klotz, S. A. et al. Degenerate peptide recognition by *Candida albicans* adhesins Als5p and Als1p. *Infect. Immun.* **72**, 2029–2034 (2004).
45. Dehullu, J., Vorholt, J. A., Lipke, P. N. & Dufrêne, Y. F. Fluidic force microscopy captures amyloid bonds between microbial cells. *Trends Microbiol.* **27**, 728–730 (2019).
46. Lipke, P. N., Klotz, S. A., Dufrene, Y. F., Jackson, D. N. & Garcia-Sherman, M. C. Amyloid-like β-aggregates as force-sensitive switches in fungal biofilms and infections. *Microbiol. Mol. Biol. Rev.* **82**, e00035 (2017).
47. Mourer, T., El Ghalid, M., d'Enfert, C. & Bachellier-Bassi, S. Involvement of amyloid proteins in the formation of biofilms in the pathogenic yeast *Candida albicans*. *Res. Microbiol.* **172**, 103813 (2021).
48. Carolus, H. et al. Diagnostic allele-specific PCR for the identification of *Candida auris* clades. *J. Fungi* **7**, 754 (2021).
49. Kim, D., Paggi, J. M., Park, C., Bennett, C. & Salzberg, S. L. Graph-based genome alignment and genotyping with HISAT2 and HISAT-genotype. *Nat. Biotechnol.* **37**, 907–915 (2019).
50. Anders, S. & Huber, W. Differential expression analysis for sequence count data. *Genome Biol.* **11**, 10 (2010).
51. Kucharíková, S., Tournu, H., Holtappels, M., Van Dijck, P. & Lagrou, K. In vivo efficacy of anidulafungin against mature *Candida albicans* biofilms in a novel rat model of catheter-associated candidiasis. *Antimicrob. Agents Chemother.* **54**, 4474–4475 (2010).
52. Reuss, O., Vik, A., Kolter, R. & Morschhäuser, J. The SAT1 flipper, an optimized tool for gene disruption in *Candida albicans*. *Gene* **341**, 119–127 (2004).
53. Carolus, H., Sofras, D., Boccarella, G. & Sephton-Clark, P. Acquired amphotericin B resistance and fitness trade-off compensation in *Candida auris*. Preprint at <https://doi.org/10.21203/rs.3.rs-3621420/v1> (2024).
54. Alsteens, D., Van Dijck, P., Lipke, P. N. & Dufrêne, Y. F. Quantifying the forces driving cell-cell adhesion in a fungal pathogen. *Langmuir* **29**, 13473–13480 (2013).
55. Alsteens, D. et al. Single-cell force spectroscopy of Als-mediated fungal adhesion. *Anal. Methods* **3**, 3657–3662 (2013).

## Acknowledgements

The work in this publication was supported by the National Institute of Allergy and Infectious Diseases of the NIH under award number R01AI130170 (NIAID) to M.A.J.-R., and NIH grant U19 AI110820 to V.M.B. This work was also supported by the University of Maryland Baltimore, Institute for Clinical & Translational Research (ICTR), the Fund for Scientific Research, Flanders, research community on biofilms (FWO #W000921N), and the Belgian National Fund for Scientific Research (FNRS). We would like to thank Miles Delmar and the UMB Electron Microscopy Core for SEM imaging and Celia Lobo Romero for excellent technical assistance. Elements of Fig. 8 were created in BioRender.

## Author contributions

M.A.J.-R. and P.V.D. conceived and designed this research, M.A.J.-R., V.M.B., and P.V.D. provided funding; T.W.W., D.M.-J., D.S., H.C., C.M., A.A. and T.O.P. performed experiments; M.A.J.-R., T.W.W., D.S., T.O.P., V.M.B., P.V.D., D.M.-J. and Y.F.D. analyzed data; M.A.J.-R., T.W.W., D.S., T.O.P., H.C., and V.M.B. wrote the paper; M.A.J.-R. oversaw the entire study. All authors read and approved the manuscript.

## Competing interests

All authors read and approved the manuscript. The authors declare no competing interests.

## Additional information

**Supplementary information** The online version contains supplementary material available at  
<https://doi.org/10.1038/s41467-024-53588-5>.

**Correspondence** and requests for materials should be addressed to Patrick Van Dijck or Mary Ann Jabra-Rizk.

**Peer review information** *Nature Communications* thanks the anonymous reviewer(s) for their contribution to the peer review of this work. A peer review file is available.

**Reprints and permissions information** is available at  
<http://www.nature.com/reprints>

**Publisher's note** Springer Nature remains neutral with regard to jurisdictional claims in published maps and institutional affiliations.

**Open Access** This article is licensed under a Creative Commons Attribution-NonCommercial-NoDerivatives 4.0 International License, which permits any non-commercial use, sharing, distribution and reproduction in any medium or format, as long as you give appropriate credit to the original author(s) and the source, provide a link to the Creative Commons licence, and indicate if you modified the licensed material. You do not have permission under this licence to share adapted material derived from this article or parts of it. The images or other third party material in this article are included in the article's Creative Commons licence, unless indicated otherwise in a credit line to the material. If material is not included in the article's Creative Commons licence and your intended use is not permitted by statutory regulation or exceeds the permitted use, you will need to obtain permission directly from the copyright holder. To view a copy of this licence, visit <http://creativecommons.org/licenses/by-nc-nd/4.0/>.

© The Author(s) 2024